

# MECHANISM OF GRAIN REFINEMENT DURING EQUAL-CHANNEL ANGULAR PRESSING IN AN Al-Mg-Sc ALLOY

S. Malopheyev, V. Kulitskiy, M. Gazizov and R. Kaibyshev

Laboratory of Mechanical Properties of Nanostructural Materials and Superalloys, Belgorod State University,  
Pobeda 85, Belgorod 308015, Russia

Received: March 22, 2016

**Abstract.** The mechanism of grain refinement of an Al-5.4Mg-0.4Mn-0.2Sc-0.09Zr alloy subjected to equal-channel angular pressing (ECAP) with a back pressure (BP) for up to 12 passes via route B<sub>c</sub> at 573K (300 °C) was studied. New grains form through a specific mechanism of continuous dynamic recrystallization (CDRX). The formation of microshear bands (MSB) enclosed by a pair of geometrically necessary boundaries (GNBs) and the splitting of initial boundaries to pairs of mutually parallel boundaries plays a vital role in initiation of recrystallization process. Transformation of the 2D lamellar structure to 3D crystallites occurs through the intersection of primary MSBs by secondary MSBs, mainly. Upon further deformation the GNBs evolve to planar sub-boundaries and then to high-angle boundaries. The formation of primary MSBs is associated with the appearance of texture  $\alpha$ -fiber, and the appearance of a new type of shear texture, which is an axial {112} texture of orientation around the transverse direction accompanies the formation of ultra-fine grains.

## 1. INTRODUCTION

The mechanism of grain refinement to the submicron-scale level during equal-channel angular pressing (ECAP) in Al and its alloys is imperfectly understood [1-11]. At intermediate temperatures, the ultra-fine grains appear uniformly over the entire volume that may occur through a mechanism of continuous dynamic recrystallization (CDRX) [2,7-10]. In general, CDRX is a one-step phenomenon including the formation of stable three-dimensional (3D) arrays of deformation-induced low-angle boundaries (LABs) due to dislocation rearrangement, followed by their gradual transformation into high-angle boundaries (HABs) [2,11]. The new grains form as a result of the increase in sub-boundary misorientation due to continuous accumulation of the dislocations introduced by the deformation [2,6,7,11]. However, Al and its alloys are materials with high stacking

fault energy (SFE) [12] and at intermediate temperatures, the rearrangement of lattice dislocations by climb and/or cross-slip followed by their mutual annihilation may hinder the formation of 3D networks of LABs [2,13]. In this condition the occurrence of CDRX is attributed to the initial development of microshear bands (MSBs) being an isolated layer referred to as the 2D type of deformation bands [2,3,7-9,14]. However, to date, the relationship between the deformation banding and grain refinement in ECAP processing is not completely understood [2,14-16]. As a result, we are far from a comprehensive physical understanding of the CDRX process in aluminum alloys during ECAP at intermediate temperatures. Authors of last overview suggested that extensive grain refinement is attained through the formation of dislocation cells followed by accumulation of lattice dislocation within

Corresponding author: S. Malopheyev; e-mail: malofeev@bsu.edu.ru

their boundaries that leads to continuous increase in their misorientation and gradual transformation of a large portion of dislocation cell walls to HABs in the low-temperature regime typical for SPD processing, i.e. below  $0.5T_m$ ,  $T_m$  is the melting temperature, [16].

Under the action of a unidirectional deformation processes the formation of lamellar structure associates with MSBs enclosed by geometrically necessary boundaries (GNBs) [2,17-21], GNBs evolve to accommodate the large strain gradients within grain interiors through self-organized glide on a single slip plane termed as planar slip [20-24]. GNBs may appear both in pairs as MSBs and in the form of separate planar boundaries with initial low-angle misorientation [17-19,21]. The arrangement of lattice dislocations in a well-defined boundary structure as a GNB instead of bundles or random arrangement of dislocations implies mutual screening of the long-range stress fields; therefore, GNBs are characterized as low-energy dislocation structures (LEDSs) [19-21]. The deformation banding introduces low-to-moderate misorientation initially. However, under certain condition the extensive plastic deformation may lead to an increase in misorientation of GNBs with strain and their eventual transformation to HABs [2,16,22].

ECAP concentrates ~ 90% of the shear strain along the intersection plane [1] that highly facilitates the formation of GNBs [23]. The initial grain orientation is a key parameter for the evolution of GNBs [17,18,21,23]. In general, in pure fcc metals, the formation of three types of dislocation boundary structures depends on the mutual orientation of a grain, and the maximum shear stress directions were reported under tension and rolling at ambient temperature [21,23,24]. It seems that GNBs may also evolve within grains with certain orientations, only [2,15]. These orientations provide a high-slip concentration in one {111} plane, i.e., coplanar slip is operative, or the activation of codirectional slip occurs on different {111} planes sharing a common <110> slip direction [19,21,23,24]. In the first case, a 2D lamellar structure appears when two active slip systems exist in one {111} plane and this process is accompanied by the appearance of the stable  $\alpha$ -fiber [11,21,23]. This lamellar structure is essentially stable up to high strains [11,21]. In the second case, the codirectional slip takes place in the grains with orientations belonging to the stable  $\alpha$ -fiber and may produce 3D network of GNBs owing to the formation of two or more sets of GNBs aligned with mutually intersecting {111} planes [24]. These GNBs are aligned with the crystallographic planes,

such as {101},  $\{3\bar{1}5\}$ , etc., which lie farther away from any {111} slip planes. The intersected lines of {111} family planes in fcc materials are either in the <110> or <123> direction, and these directions may lie on the intersection between active {111} slip planes and a boundary plane [23,24]. The interactions between non-coplanar sets of MSBs leads to subdivision of primary MSBs by secondary or tertiary MSBs into crystallites with nearly rectangular shape [17,24]. No such detailed analysis was performed for ECAP.

In the Cube grains [11] oriented for easy cross slip on four {111} planes with no favored slip system, codirectional slip induces cells without GNBs [22,23]. This grain orientation is unstable under rolling and rotates away to a stable orientation due to an imbalance of slip activity between three or more active slip systems [23,24]. The formation of GNBs may occur in these grains with strain due to the transition from multiple slip to predominantly coplanar slip in one {111} plane [24]. MSBs delimited by these GNBs and aligned with the {111} plane of a dominant coplanar slip penetrate into the cell structure. In addition, dislocation cells may elongate and coalesce in a self-organized manner after the appearance of a highly stressed slip system, which provides the evolution of cell structure into a bamboo-like structure [11,17]. Simple shear facilitates this process as under torsion [25].

Under warm-to-hot working conditions ( $0.5\div 0.6 T_m$ ), the self-organized dislocation glide, cross-slip and climb provide the formation of GNBs as regular dislocation arrangements, i.e., in the form of planar sub-boundaries [15,26]. The long-range stress fields originating from initial GNBs are high enough to prevent the entry of gliding dislocations into the boundary hindering the continuous increase in their misorientation up to ~ 15° [15,19,22]. In contrast, a planar sub-boundary induces a low long-range stress field [11] that facilitates trapping mobile lattice dislocations and provides a high rate of misorientation increase with strain [7-10]. Mobile dislocations moving across the sub-grains are easily forced into the sub-boundaries [7]. Therefore, the formation of planar sub-boundaries is a necessity condition for their subsequent transformation to HABs with a high rate [7,15].

The aim of this study is to establish the regularities of the grain refinement process in an Al-Mg-Sc-Zr alloy denoted as 1570C Al [27] with a high SFE containing a dispersion of the  $Al_3(Sc,Zr)$  ( $L1_2$ ) phase in a ECAP with a back pressure (BP) using route  $B_c$  at 573K (300 °C) [1,12]. Previous works on Al-Mg alloys with nearly the same chemical

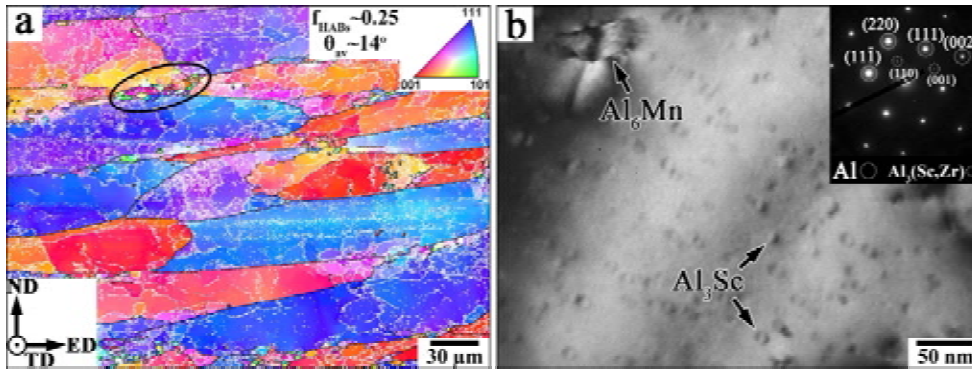


**Fig. 1.** Initial microstructure after hot extrusion: (a) EBSD map and (b) TEM micrograph. In (b), diffraction pattern in the top right corner illustrates coherent nature of  $\text{Al}_3(\text{Sc,Zr})$  precipitates.

composition distinguished by a dispersion of coherent particles showed that grain refinement during ECAP in this type of Al-Mg alloy associates with CDRX occurrence [10,13,14]. Under warm working at 573K (300 °C), the dislocation climb is operative in Al-Mg alloys [28], which is important for the aforementioned evolution of GNBs in the form of planar sub-boundaries [7,15,26]. A BP was applied to ensure the integrity of samples at high strains and the homogeneity of deformation during ECAP [1,29,30]. Route  $B_c$  offers the most efficient strain path changes under ECAP [1], which provides the best condition for the formation of 3D networks of GNBs [15,29].

## 2. MATERIAL AND EXPERIMENTAL PROCEDURE

The 1570C Al alloy, with a chemical composition of Al-5.41Mg-0.37Mn-0.29Ti-0.2Sc-0.09Zr-0.07Fe-0.04Si (in weight %), was manufactured by direct chill casting followed by homogenization annealing at 633K (360 °C) for 8 h and extrusion at an initial temperature of 653K (380 °C) with a ~75% reduction in cross section, which is equal to a true strain of ~1.3. The samples were machined from the central part of the billet parallel to the extrusion direction. Details of ECAP processing were reported in previous works [15,29].

The specimens for microstructural examination were cut from the central parts of the pressed rods in the longitudinal direction parallel to the last pressing direction [15]. Samples for EBSD analysis were electropolished using a standard 25%  $\text{HNO}_3$  + 75%  $\text{CH}_3\text{OH}$  solution at 241K (-32 °C) and 19.5 V to produce a strain-free surface [29]. The EBSD analysis was performed using an FEI Quanta 600FEG SEM equipped with a high-resolution electron backscatter analyzer [28]. All EBSD maps

were oriented along the last pressing direction. HABs and LABs were defined when adjacent pixels in the map have a misorientation of  $>15^\circ$  and  $2^\circ < \theta \leq 15^\circ$  and depicted in misorientation maps using black and white lines, respectively [7,15,29]. Terms of grain and subgrains referred to crystallites entirely delimited by HABs, LABs, while (sub)grains are bounded partly by LABs and partly by HABs [10,15,29]. The examination area was automatically scanned in 100-nm steps. Samples for TEM examinations were mechanically thinned and then electropolished using the aforementioned solution and a Tenupol-5 twinjet polishing unit. The dislocation density was estimated by counting individual dislocations crossing the thin foil surface [7,31]. The misorientations on the LABs were additionally studied using a conventional Kikuchi-line technique [31]. Texture measurements on macroscale structural level were carried out by X-ray diffraction using an ARL X'TRA diffractometer. Samples parallel to the Y-plane (Fig. 1) [15,32] were taken from the mid-section of the materials. (111), (200), (220) and (311) pole figures were obtained and orientation distribution functions (ODF) were calculated using MTEX software.

## 3. EXPERIMENTAL RESULTS

### 3.1. Initial microstructure

The average dimensions of initial grains in the extrusion direction and normal directions were ~ 93 and ~ 30  $\mu\text{m}$  (Fig. 1a), respectively. Sub-grains delimited by LABs with very low misorientation were observed within these grains. As a result, the fraction of LABs with low misorientation in the range from 2 to 4° is ~ 52%. The fraction of HABs was ~ 25%, and the average misorientation was 14°. The volume of the recrystallized grains with an elongated shape

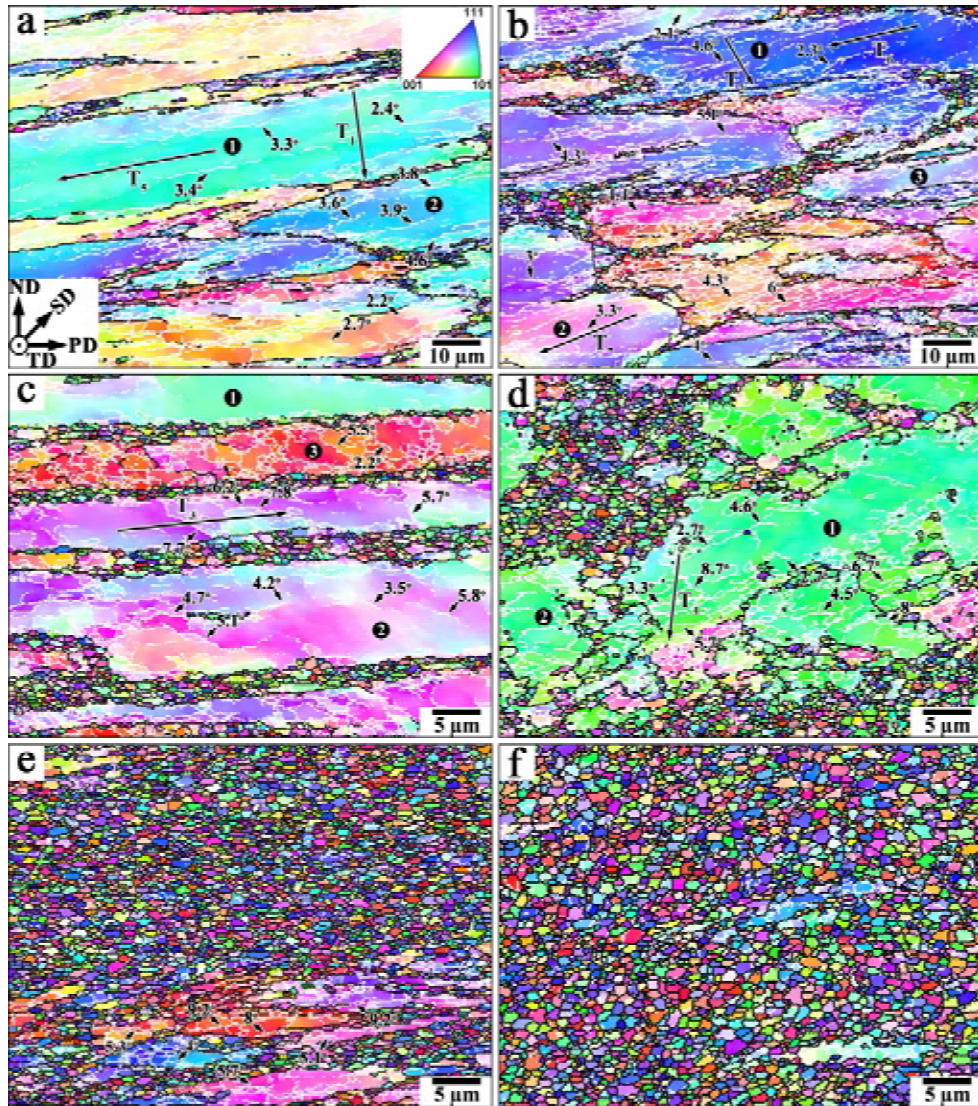


**Fig. 2.** Typical EBSD maps of ECAPed 1570C Al at: (a)  $\varepsilon \sim 1$ , (b)  $\varepsilon \sim 2$ , (c)  $\varepsilon \sim 4$ , (d)  $\varepsilon \sim 6$ , (e)  $\varepsilon \sim 8$ , and (f)  $\varepsilon \sim 12$ .

is negligible  $\sim 0.02$  (delineated area in Fig. 1a). These grains were observed along the initial boundaries; their average dimensions in the longitudinal and normal directions were  $\sim 7.6$  and  $2.7 \mu\text{m}$ , respectively. The density of the lattice dislocations within the original coarse grains was measured to  $\sim 1 \times 10^{13} \text{m}^{-2}$ .

Two types of nanoscale dispersoids were observed. Coherent  $\text{Al}_3(\text{Sc,Zr})$  dispersoids having a size of  $\sim 10 \text{nm}$  were uniformly distributed, and round  $\text{Al}_6\text{Mn}$ -phase particles with an average size of  $\sim 40 \text{nm}$  were occasionally observed within the grains (Fig. 1b). The coffee-bean contrast and orientation relationship (see the diffraction pattern in the top right corner of Fig. 1b) confirm the coherent nature of the  $\text{Al}_3(\text{Sc,Zr})$  dispersoids. Note that  $\text{Al}_6\text{Mn}$  particles were easily distinguishable by the size and origin of the interface boundaries.

### 3.2. Deformation microstructure

Typical EBSD maps, misorientation distributions, and TEM micrographs of the deformation microstructures are shown in Figs. 2, 3, and 4, respectively. Misorientation variations within unrecrystallized areas of initial grains are shown in Fig. 5 as the point-to-point or point-to-origin misorientations along the  $T_x$  lines indicated in Fig. 2. Fig. 6 summarizes the following: the effect of strain on the boundary spacing determined via the EBSD (a) and TEM (b) techniques; the average size of the DRX grains,  $d$ , (c); the fraction of HABs,  $V_{\text{HAB}}$ , and the average misorientation,  $\theta_{\text{av}}$ , (d), the fraction of recrystallized grains,  $V$ , and the dislocation density,  $\rho$ , (e); and the misorientation obtained by TEM (f). The orientations of round areas with diameters of the marked black circles in Figs. 2a-d

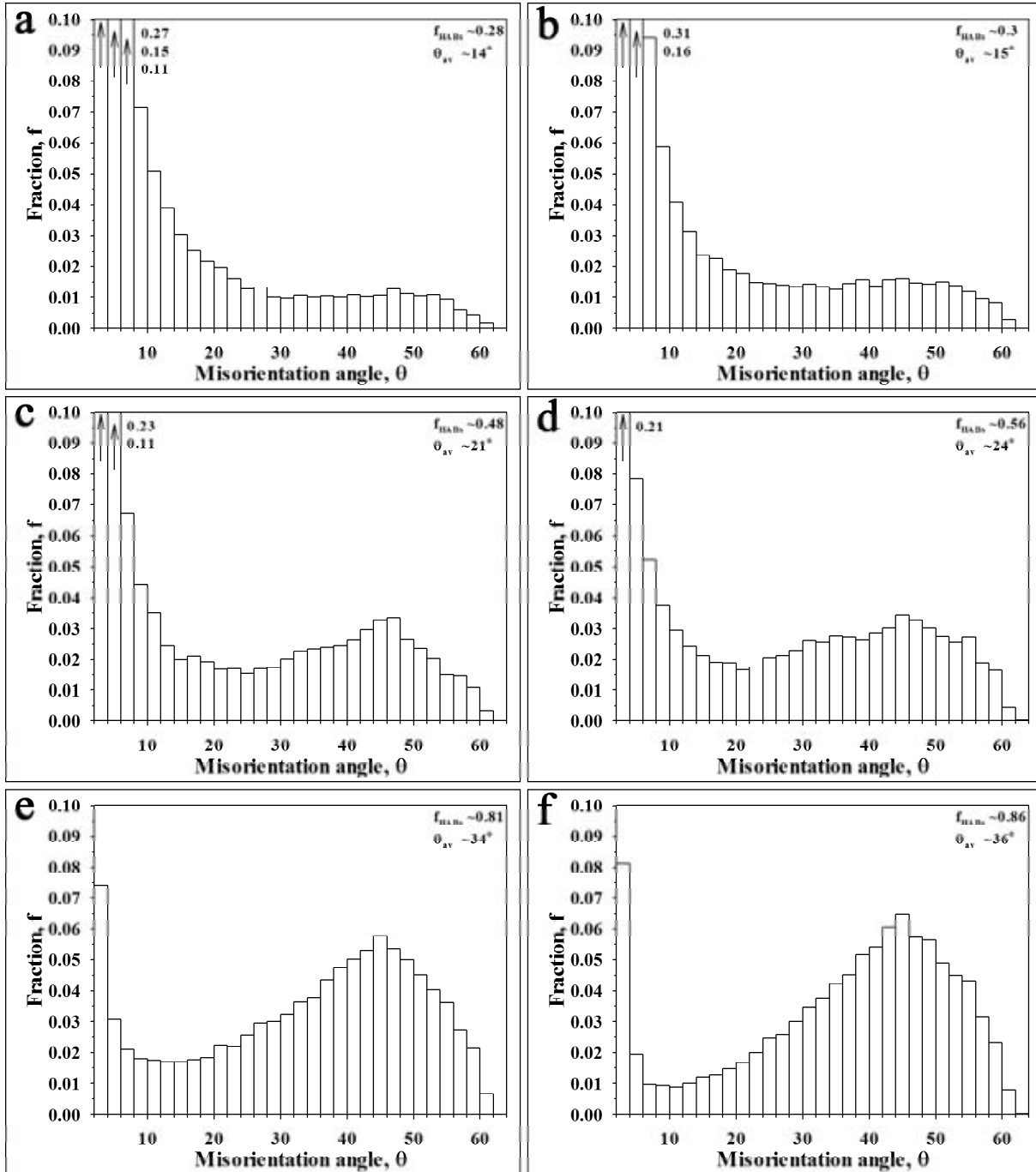


**Fig. 3.** Effect of strain on the misorientation distribution: (a)  $\epsilon \sim 1$ ; (b)  $\epsilon \sim 2$ ; (c)  $\epsilon \sim 4$ ; (d)  $\epsilon \sim 6$ ; (e)  $\epsilon \sim 8$ , and (f)  $\epsilon \sim 12$ .

are represented on the  $\{111\}$  pole figures (Fig. 7) reconstructed from EBSD data obtained for mesoscale structural level (Fig. 2).

For  $\epsilon \sim 1$ , extended planar boundaries with an average misorientation of  $\sim 4^\circ$  and a large fraction of the straight segments with high-angle misorientation evolve within initial grains (Fig. 2a). Values of  $V_{HAB}$  and  $\theta_{av}$  increase to  $\sim 28\%$  and  $13.7^\circ$ , respectively (Figs. 3a and 6d). Both the initial boundaries and the planar LABs tend to align at an

angle of  $\sim 20^\circ$  to the pressing direction (PD) (Fig. 2a). This angle is essentially equal to the inclination angle ( $\sim 22.5^\circ$ ) of an initial spherical element deformed into an ellipsoid [32] and, therefore, a crystallite delimited by initial boundaries and deformation-induced planar LABs deforms as a whole specimen. The pair of an initial boundary and a deformation-induced planar boundary forms a ribbon, which is subdivided by straight transverse LABs into sub-grains and/or (sub)grains (Fig. 4a).

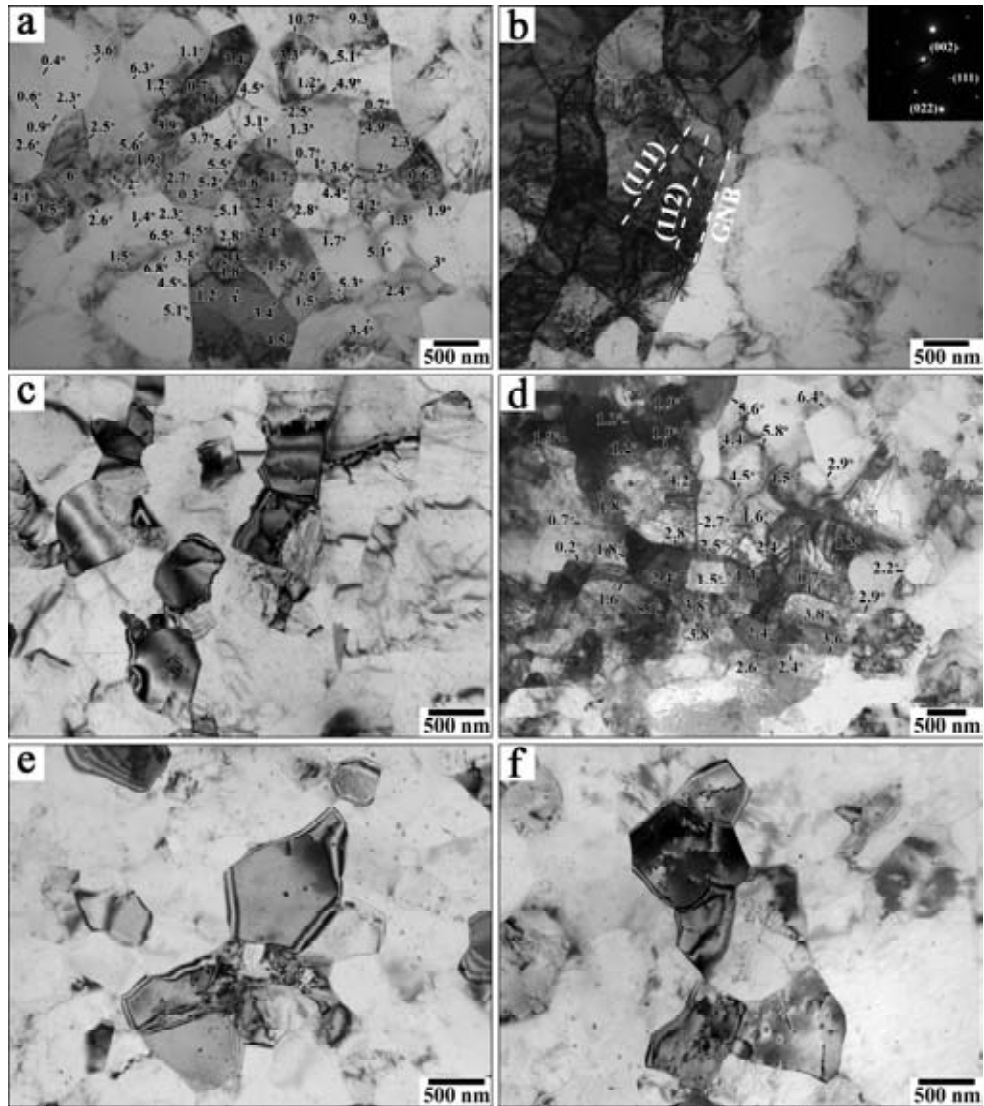
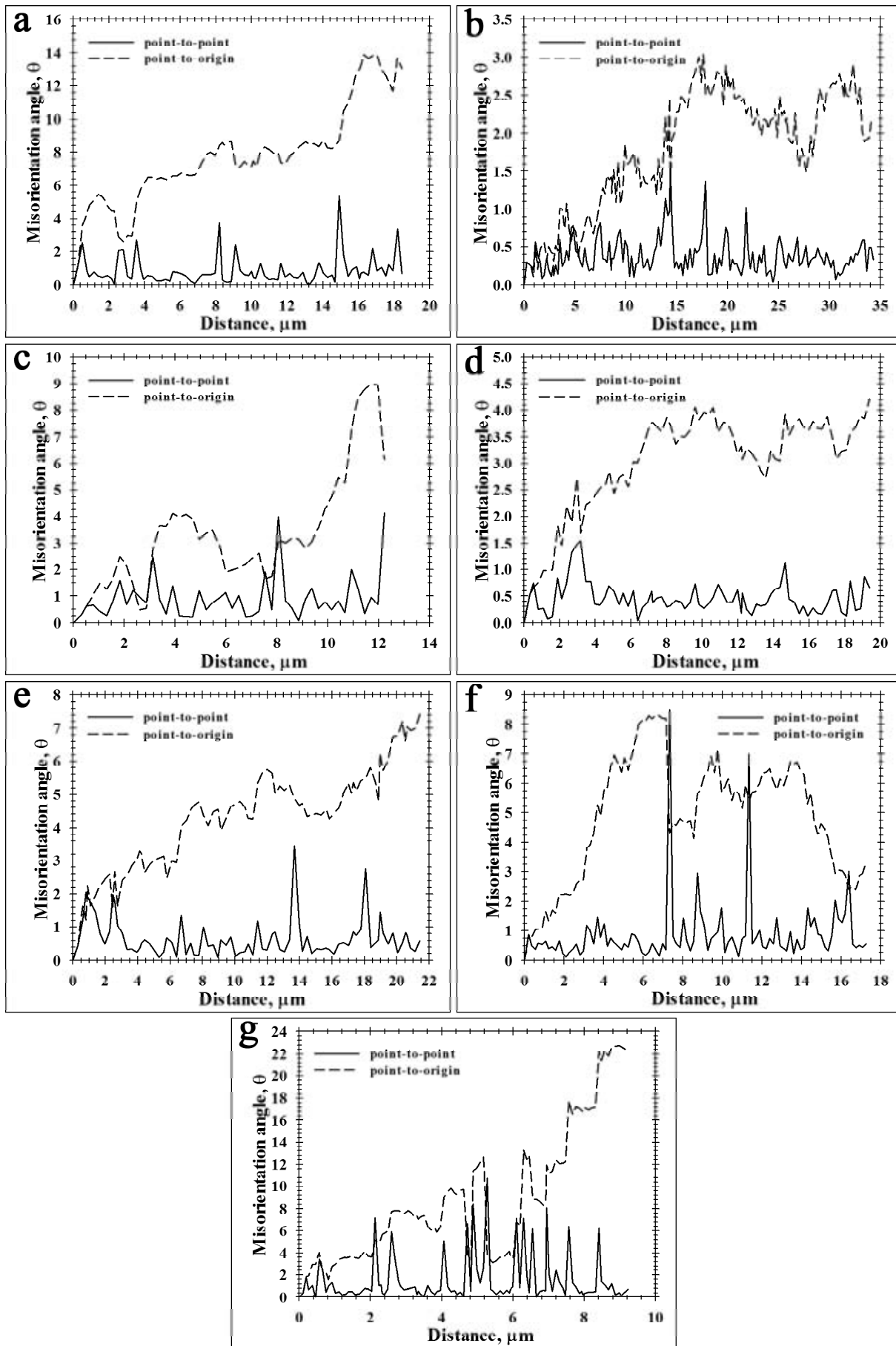


Fig. 4. TEM images of ECAPed 1570C Al at: (a,b)  $\epsilon \sim 1$ , (c)  $\epsilon \sim 2$ , (d)  $\epsilon \sim 4$ , (e)  $\epsilon \sim 8$ , and (f)  $\epsilon \sim 12$ .

The formation of this pair could be attributed to the stress-driven splitting of an initial boundary trapped a high number of mobile lattice dislocations [33]. The average misorientation of the longitudinal LABs is higher than the average misorientation of the transverse LABs (Figs. 2a and 4a). In addition, subgrains with nearly rectangular shape and outlined by LABs are formed (Figs. 4a and 6b). Extended planar boundaries evolve in grain orientations belonging to  $\alpha$ -fiber (no. 1 in Fig. 2a) or  $\beta$ -fiber (no. 2 in Fig. 2a) (Fig. 7a) [32].

Misorientation variations within a deformed grain with orientation belonging to  $\alpha$ -fiber [32] (Fig. 7a) that are perpendicular ( $T_1$ ) and along ( $T_2$ ) with the shear direction (SD in Fig. 4) show significant strain gradients associated with continuous lattice rotations over a rather large distance of  $\sim 20 \mu\text{m}$  (Figs. 5a and 5b). The net Burgers vector

perpendicular to the SD is higher by a factor of  $\sim 5$  than along this direction. The lattice rotations are partially concentrated in the planar boundaries with average misorientations of  $\sim 4^\circ$  and  $\sim 1^\circ$  located along and perpendicular to the SD, respectively (Figs. 2a, 5a, and 5b). Therefore, the planar extended boundaries could be interpreted in terms of GNBs [19,21]. The alignment of a GNB with the  $\{111\}$  slip plane occurs with large inclination angles close to  $15^\circ$  (Fig. 4b). In contrast, the GNB aligns with the  $\{112\}$  slip plane with small inclination angles less than  $2^\circ$ , and therefore, it is apparent that the boundary plane belongs to the  $\{112\}$  family (Fig. 4b). This boundary plane was not predicted from theoretical consideration of GNB alignment under unidirectional deformation processes [21,23,24]. The dislocation density increases up to  $\rho \sim 4 \times 10^{13} \text{ m}^{-2}$  (Fig. 6e).



**Fig. 5.** The misorientation variations are shown for the distance along the lines of (a)  $T_1$ , (b)  $T_5$ , (c)  $T_2$ , (d)  $T_6$ , (e)  $T_7$ , (f)  $T_3$ , (g)  $T_4$  in the OIM micrographs having the same definitions as those in Figs. 4a, 4b, 4c, and 4d, respectively.

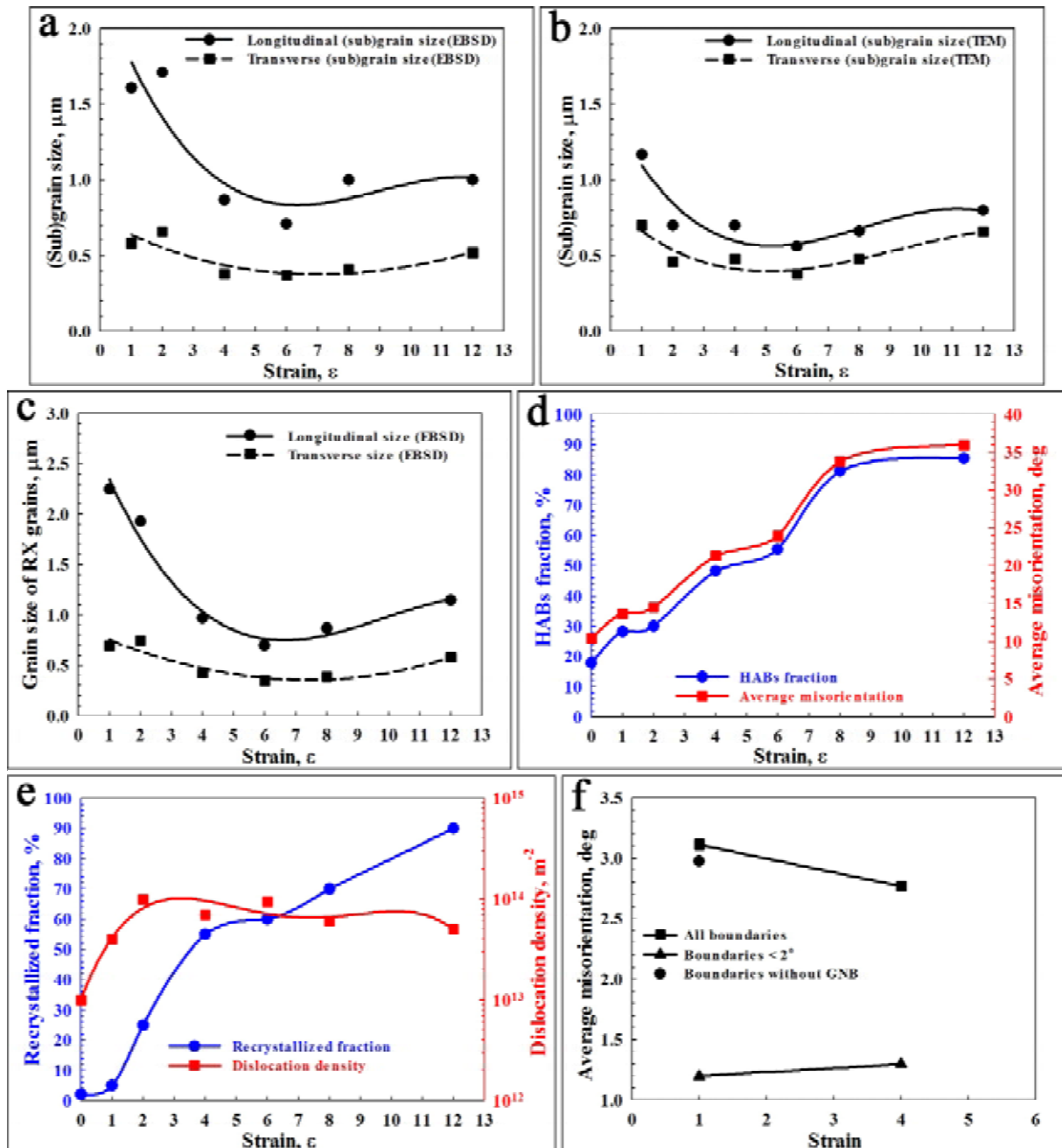


**Fig. 6.** Effect of strain on (a) (sub)grain size determined by EBSD technique; (b) (sub)grain size determined by TEM technique; (c) grain size determined by EBSD technique; (d) HABs fraction and average misorientation; (e) recrystallized fraction and dislocation density; (f) the average misorientation from TEM data.

For  $\epsilon \sim 2$ , numerous fine and straight MSBs appear, resulting in a significant increase in the number of planar GNBs with an average misorientation of  $\sim 4^\circ$  (Fig. 2b). These boundaries have no sense relative to the initial boundaries. Their appearance in parallel and near the initial boundaries or pairs of GNBs develops lamellas. The ribbons evolved after the first pass convert to chains of recrystallized grains through the generation of

individual (sub)grains or even grains by intersecting secondary planar GNBs. The formation of new GNBs and chains of recrystallized grains leads to subdivision of the initial grains with orientations belonging to  $\beta$ -fiber, primarily to separate areas (Figs. 2b and 7b). Superposition of the transformation of the ribbons to chains of recrystallized grains, which rarely occurs at this strain, with the extensive formation of new planar LABs leads to the

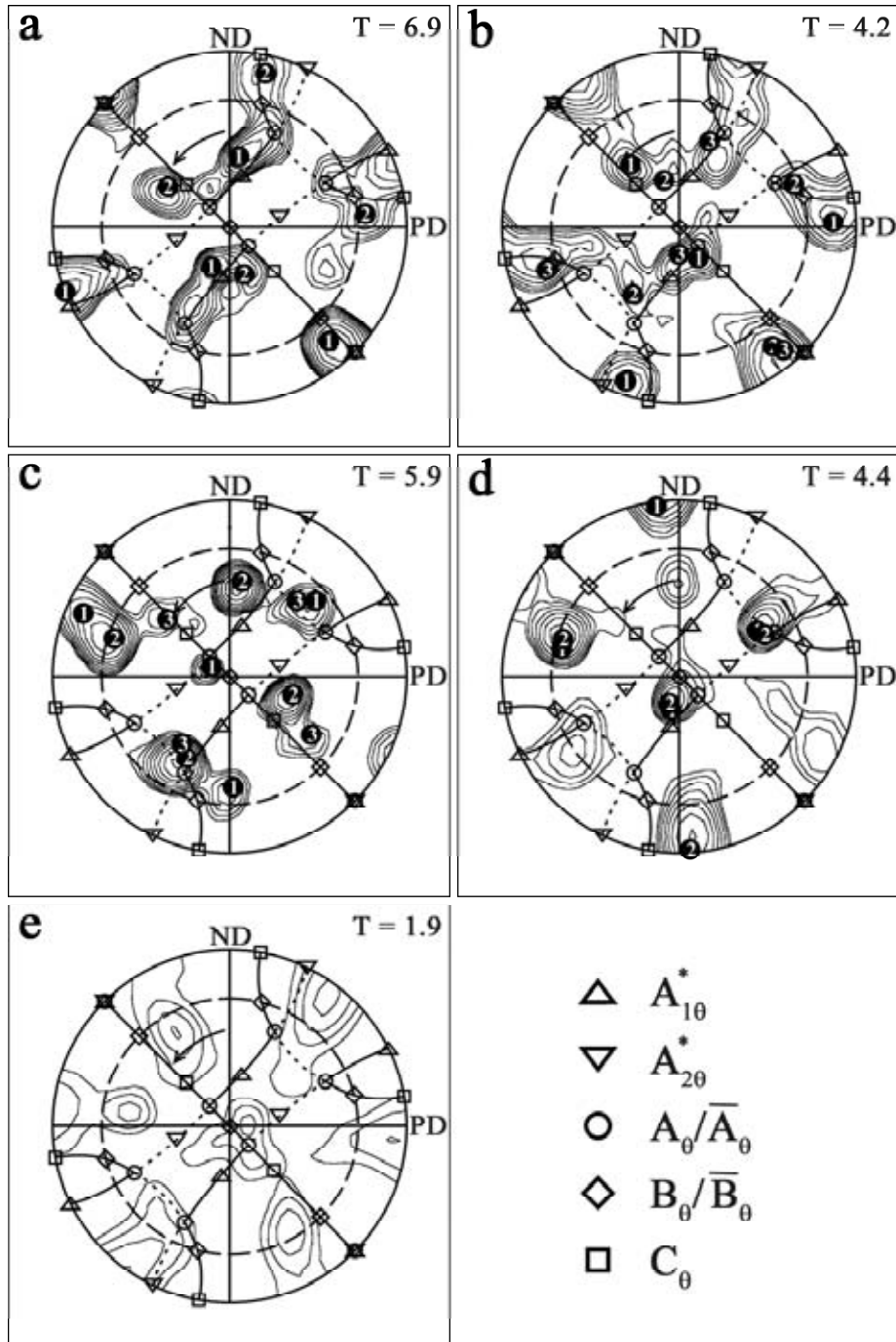


**Fig. 7.** {111} pole figures of 1570C processed to (a) 1, (b) 2, (c) 4, (d) 6, and (e) 8 ECAP passes.  $T$ —texture index. Contours: 1/1.3/1.7/2.2/2.8/3.6/4.6/6/7.7/10. The ideal orientations and fibers of simple shear textures for an fcc metal are marked.  $\gamma$ -fiber are marked by long dash line circle.

appearance of plateaus on strain dependencies of the  $V_{HAB}$  and  $\theta_{av}$  values and no variation in dimensions of subgrains and (sub)grains outlined by boundaries with misorientation  $\geq 2^\circ$  (Figs. 3b, 6a, and 6d). Concurrently, the size of the subgrains bounded by LABs with misorientation  $< 2^\circ$  decreases (Figs. 4c and 6b). Strain gradients within unrecrystallized grains associated with continuous

lattice rotations increase by a factor of approximately 3, and the average LAB spacing decreases (Figs. 5c, 5d, and 5e). Therefore, dislocation tensor highly increases with strain, indicating the great polarity of the accumulated dislocations. In contrast with the first pass, these strain gradients along ( $T_6$  and  $T_7$ ) and perpendicular ( $T_2$ ) to the SD (Fig. 2b) become essentially the same (Figs. 5c, 5d, and 5e).

Therefore, the strain path change in route B<sub>c</sub> provides an isotropic net Burgers vector within unrecrystallized remnants. The density of the lattice dislocations increases up to  $\rho \sim 1.2 \times 10^{14} \text{ m}^{-2}$  and insignificantly decreases upon further strain (Fig. 6e). Note that the dislocation density within the unrecrystallized remnants, new grains, or (sub)grains is the same (Fig. 4c). It is apparent that at  $\varepsilon > 2$ , a dynamic equilibrium between the number of dislocations emitted by the sources and the number of dislocations trapped by the boundaries is established, and no change in dislocation density occurs.

For  $\varepsilon \sim 4$ , a partially recrystallized structure was observed (Fig. 2c). The formation of new grains is strongly dependent on the orientation of the initial grains (Fig. 2c). In orientations belonging to the stable  $\alpha$ - and  $\beta$ -fibers [32], the chains of recrystallized grains increase their thickness (no. 3 in Figs. 2c and 7c). Ribbons enclosed by new planar GNBs appear in parallel to the existing necklace. These lamellas tend to transform into the chains of recrystallized grains through the conversion of transverse LABs to HABs (Fig. 2c). As a result, steep increases in the  $\theta_{av}$  and  $V_{HAB}$  values occur (Fig. 6d). Well-defined 3D networks of LABs are retained within some unrecrystallized remnants with orientations deviated from the stable fibers (nos. 1 and 2 in Figs. 2c and 7c). The average misorientations of longitudinal and transverse boundaries of these equiaxed subgrains become essentially the same (Fig. 2c). Misorientation of these boundaries is low ( $\sim 2^\circ$ ) and independent of strain (Fig. 6f), which allows their interpretation as incidental dislocation boundaries (IDB) [19]. No remarkable formation of new IDBs occurs in the strain interval 2-4; as a result, the size of subgrains remains unchanged (Figs. 6a and 6b).

The strain gradients within unrecrystallized areas significantly increase (Figs. 2c and 5f). As a result, unrecrystallized remnants are subdivided by high dense GNBs with a misorientation of  $\sim 8^\circ$  (Fig. 5f). Different slip patterns appear on each side of a GNB if misorientation of this boundary becomes  $\geq 4^\circ$ . These GNBs easily convert to HABs with a high rate upon further strain. Orientations of grains containing 3D networks of boundaries with moderate-to-high misorientation (no. 3 in Fig. 2c) belong to  $\beta$ -fiber (Fig. 7c). Orientations containing low dense planar GNBs (nos. 1 and 2 in Fig. 2c) are deviated from the stable orientations (Fig. 7c).

At  $\varepsilon > 2$ , the formation of MSBs followed by their transformation to chains of recrystallized grains leads to subdivision of unrecrystallized remnants

(Figs. 2c-e). It is apparent that certain unstable grain orientations locating close to  $\alpha$ -fiber with tilts [32] ranging from  $10$  to  $20^\circ$  are resistant to the appearance of GNBs (Figs. 2b-2d and 7c-7d). The penetration of GNBs in 3D networks of IDBs followed by the subsequent transformation of the ribbons to chains of recrystallized grains with strain is the main process of microstructural evolution in these orientations (Figs. 2b-2d and 4c-4e). In the strain interval 4-8, this process occurs continuously and leads to a high rate increase in the  $\theta_{av}$  and  $V_{HAB}$  values and a shift of the misorientation distribution toward high-angles with strain (Figs. 3c-3e and 6d), while no remarkable formation of new LABs with misorientation  $< 4^\circ$  occurs (Figs. 4c-4e). As a result, at  $\varepsilon \geq 8$ , the fraction of the LABs with misorientation of value  $\leq 4^\circ$  decreased to  $\sim 0.1$ , and the partially recrystallized structure eventually converts to fully recrystallized structure at  $\varepsilon \sim 12$  (Fig. 2f). In the strain interval 8-12, the sizes of the grains and (sub)grains slightly increase with strain (Figs. 6a and 6b), and an essential saturation of the  $\theta_{av}$  and  $V_{HAB}$  values occurred (Fig. 6d). Most of the boundaries revealed via the TEM technique have high-angle origin at  $\varepsilon \geq 8$  (Figs. 4e and 4f), and the misorientation distribution becomes close to the theoretical one [34] for HABs discarding the low-angle peak (Figs. 3e and 3f).

Deformation-induced boundaries were nearly free of grain boundary dislocations (Fig. 4f). No changes in the average sizes of the  $\text{Al}_3(\text{Sc,Zr})$  and  $\text{Al}_6\text{Mn}$  particles were found (Fig. 4). Note that the inclination angle between extended planar boundaries and the last shear direction tends to increase with strain (Figs. 2c and 2d) up to  $\sim 27^\circ$  that is typical for the distortion of initial cubic elements under shear in ECAP die [1,15,32].

### 3.3. Texture evolution

Fig. 8 shows the ODFs for the initial and deformed material. The ideal ECAP orientations and fibers of simple shear textures for an fcc metal [32] are marked. The typical texture of extruded fcc material with a high value of SFE is observed in the initial state (Fig. 8a). The texture index is relatively low ( $\sim 2.6$ ). For  $\varepsilon \sim 1$ , the texture index increases to  $\sim 4.4$  and the intensities of the  $A_0 / \bar{A}_0$ , as well as  $A_0 / \bar{A}_0$  the components are essentially the same (Fig. 8b), which suggests that monoclinic symmetry was achieved in the first pass [31]. The strong  $\{111\}$ /Shear Plane  $\alpha$ -fiber can be identified [32]. The  $A_{10}^+$  orientation is the strongest component, whereas the  $C_0$  and  $A_{10}^-$  components are weaker. Large tilts of

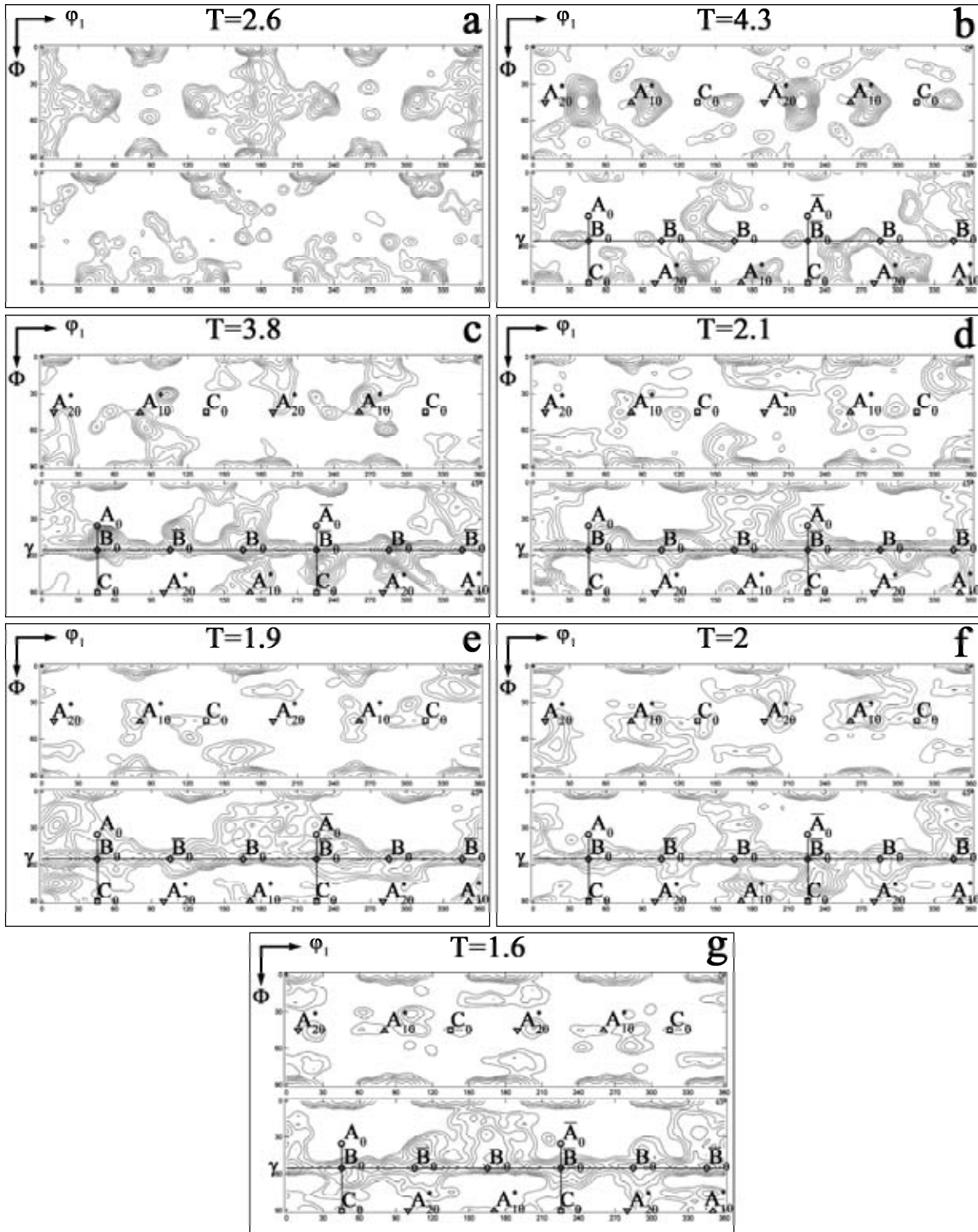


**Fig. 8.** ODFs (at section  $\varphi_2 = 0^\circ$  and  $45^\circ$ ) of 1570C Al in (a) initial state and processed to (b) 1, (c) 2, (d) 4, (e) 6, (f) 8, and (g) 12 ECAP passes. Contours: 1.4/2/2.8/4/5.6/8/11/16/22/29.  $T$  – texture index. It is worth noting that these two sections contain all the ideal components and the entire  $\beta$ -fiber (in the  $\varphi_2 = 45^\circ$  section), but not the whole  $\alpha$ -fiber [27]. (see Section 3.3 for details).

components belonging to the  $\alpha$ -fiber exist. The  $A_{20}^*$ ,  $C_0^*$ , and  $A_{10}^*$  orientations deviated from the expected theoretically ideal positions by as much as  $30^\circ$ ,  $\sim 25^\circ$  and  $\sim 15^\circ$ , respectively. Such large anisotropic deviations could not be attributed to deviations from

the condition of ideal simple shearing because the material body was rigid and the die has very sharp inner and outer corners [32]. Moreover, the BP was applied. Therefore, the most probable reason for such large tilts, which are different for different

components, is work hardening accompanied by anisotropy of the mechanical properties attributed to deformation banding [32]. In contrast, tilts of the  $B_0 / \bar{B}_0$  components are less than  $10^\circ$ . No formation of the continuous  $\beta$ -fiber was detected.

After the second pass, the initially monoclinic symmetry is nearly lost, and the texture index slightly decreases to  $\sim 3.8$  (Fig. 8c). The appearance of numerous orientations, which are unstable in shear, is the main feature of texture at  $\varepsilon \geq 2$ . There is no evidence for the formation of both the continuous  $\alpha$ - and the  $\langle 110 \rangle // \text{Shear Direction}$   $\beta$ -fibers [32]. Only the stable texture components belonging to these fibers evolve. The intensity of the  $A_{10}^*$  and  $A_{20}^*$  texture components weakened, and the  $C_0$  components disappeared. The tilts of the  $A_{10}^*$  and  $A_{20}^*$  texture components are  $\sim 15^\circ$ . The main feature is the formation of a continuous line of orientations at  $\Phi = 54.74^\circ$ ,  $\varphi_2 = 45^\circ$ , and  $\varphi_1 = 0-360^\circ$  in Euler space. This tube involves the  $B_0 / \bar{B}_0$  texture components and can be referred to as  $\gamma$ -fiber [15]. Note that the present  $\gamma$ -fiber corresponds to rotational symmetry of the  $\{112\}$  planes around the Y-axis (TD) and has no relation to the well-known  $\gamma$ -fiber corresponding to the orientations of the  $\{111\}$  planes parallel to the rolling plane [11]. The  $B_0 / \bar{B}_0$  orientations are strongest, but the intensity of the unstable segment of the continuous  $\gamma$ -fiber is only slightly weaker (Figs. 8c-8g). In general, this fiber is not stable in shear, and only the  $B_0 / \bar{B}_0$  texture components are stable in it [32]. Despite this fact, at  $\varepsilon \geq 2$ , the well-defined  $\gamma$ -fiber evolves after each pass as the main texture fiber and only slightly weakens with strain (Figs. 8c-8g). Notably, the continuous  $\gamma$ -fiber is depicted on the ODF taken from a relatively large material volume, while only separate orientations close to the ideal  $B_0 / \bar{B}_0$  components are depicted on the pole figures (Fig. 7) obtained from small material volumes. No continuous rings including the ideal  $B_0 / \bar{B}_0$  components were revealed on the  $\{111\}$  pole figures after any passes (Fig. 7).

Upon further strains, the weights of stable orientations increase and the unstable orientations tend to disappear, except the ones belonging to the  $\gamma$ -fiber (Figs. 8d-8f), which is in contrast with the evolution of texture at lower strains. At  $\varepsilon \sim 4$ , the weak  $C_0$  component reappears with a tilt of  $\sim 15^\circ$ , and the  $A_{20}^*$  and  $A_{10}^*$  texture components disappear and become weak (Fig. 8d). At  $\varepsilon \geq 6$ , the poorly defined  $\beta$ -fiber appears (Figs. 8e-8g), and at  $\varepsilon \geq 8$ , all texture components belonging to the  $\alpha$ -fiber are distinguished (Figs. 8f and 8g). Tilts of the  $A_{10}^*$ ,  $A_{20}^*$ , and  $C_0$  components become less than  $10^\circ$ . All of

the texture components except  $B_0 / \bar{B}_0$  orientations are weak (Figs. 8e-8g); randomization of texture occurs at high strains. The texture index ranges from 1.6 to 2.

#### 4. DISCUSSION

A distribution of coherent particles effectively suppresses discontinuous grain coarsening during static annealing between ECAP passes [10,13]. The 1570C alloy indeed undergoes CDRX under warm ECAP since the misorientation distribution eventually shifts from low-angle to high-angle with strain (Fig. 3), the size of new subgrains/(sub)grains/grains decreases strongly up to  $\varepsilon \sim 4$  and then increases slowly to reach a steady value at large strains (Figs. 6a, 6b, and 6c), a strong crystallographic texture forms (Figs. 7 and 8) [2,7-10,15,35]. The formation of a necklace structure of new grains through CDRX [11] rather than discontinuous DRX [2,36] is attributed to superposition three factors. First, there is a large difference between the initial grain size and the recrystallized grain size of  $\sim 60$  (Figs. 1 and 2) [11]. Second, a gradient of continuous misorientation from the grain center to pre-existing grain boundaries exists (Fig. 5) [1]. This gradient clearly increases progressively with an approaching initial boundary (Figs. 5a and 5b). Third, the splitting of initial boundaries aligned along shear direction leads to the formation of ribbons which are subdivided by transverse boundaries to ultra-fine grains after two passes [33,37].

At intermediate temperature of  $\sim 0.67T_m$ , LABs evolve easily. The final formation of fully recrystallized structure requires very large strain, despite the fact that the transformation of LABs with misorientation  $> 4^\circ$  to HABs occurs with a high rate. The low rate of grain refinement is attributed to the fact that most of the LABs evolved after the first and second passes are IDBs, and GNBs having misorientation  $> 4^\circ$  initially are in the strong minority. These boundaries could be split to separate mobile boundaries consisting of dislocation with opposite Burgers vector, separate dislocation or annihilated due to interaction of intrinsic and extrinsic dislocations with opposite Burgers vector [11,37,38]. As a result, portion of these boundaries grows slowly with strain (Fig. 3). Indeed, the overall rate of CDRX is controlled by the formation of 3D arrays of GNBs because only these boundaries are immobile and able to increase their misorientation with strain due to trapping mobile lattice dislocations (Fig. 6f). This process is strongly dependent on the initial grain orientations.

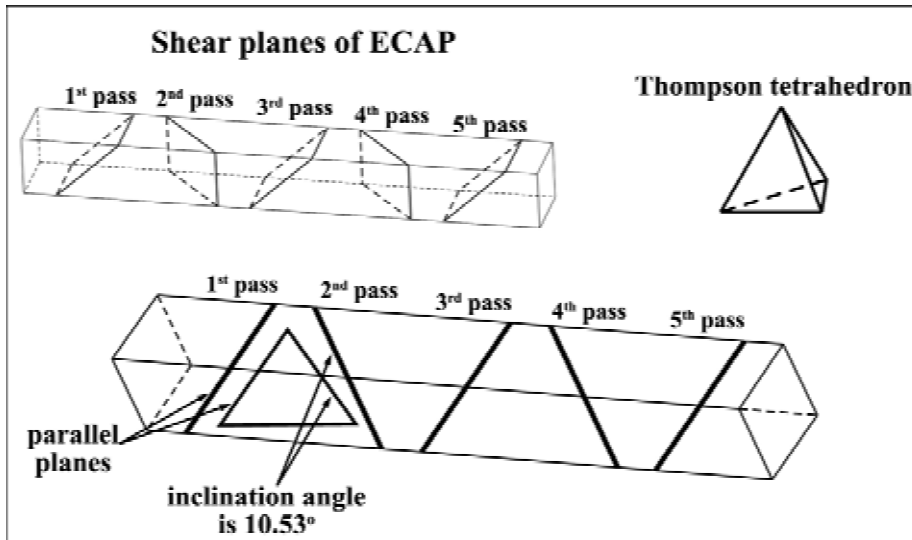


**Fig. 9.** Schematic illustration of the shear patterns in route  $B_C$ , and angles between the ECAP shear planes and  $\{111\}$  families of Thompson tetrahedron.

In grains belonging to the  $\alpha$ -fiber after the first pass the alignment of the initial boundaries and extended planar GNBs along the most stressed  $\{111\}$  plane occurs, concurrently, and directional ribbon grain structure denoted as Type 1 evolves after the first pass. Their subsequent segmentation to chains of subgrains occurs through the intersection of ribbons by the secondary MSBs, mainly in following way [15]. The  $\{111\}$  plane, which was most stressed on the first pass, could not be reoriented at an angle of  $90^\circ$  on the second pass to retain the most stressed one again (Fig. 9). This angle is too high for reorientation. At the same time, on the second pass, there is an  $\{111\}$  plane that was not the most stressed plane on the first pass and can be easily reoriented because the angle between this plane and the die shearing plane is reasonably low ( $10.53^\circ$ ). Upon the second pass, slip concentration occurs in this plane, which leads to the appearance of the secondary MSBs penetrating the existing ribbons [15]. Interaction of long-range stress fields originated from GNBs containing a high density of extrinsic dislocations and belonging to different families makes these boundaries immobile [37]. As a result, chains of recrystallized grains start to appear after the second pass (Fig. 2b). However, dislocation substructures consisting of high density of both individual dislocations and 3D networks of IDBs with misorientation of  $\sim 3^\circ$ , which may play a role of conventional HABs in strain hardening [39], preventing the concentration of dislocation glide in one  $\{111\}$  plane within an initial grain. The formation of tertiary MSBs is hindered; thus, no well-defined

$\alpha$ -fiber reappears. As a result, the subdivision of ribbons to (sub)grains may occur at  $\varepsilon > 2$ , mainly due to the transformation of GNBs evolved at previous passes to HABs. This process leads to conversion of lamellar structure to chains of recrystallized grains.

In the initial grains with orientations deviating from the stable  $\alpha$ - and  $\beta$ -fibers the multiple slip produces Type 2 structure [21,23]. IDBs with very low misorientation trap dislocations having nearly zero polarization, which effectively prevents an increase in their misorientation (Fig. 6f). Gliding dislocations are trapped by these LABs and may annihilate with dislocations having opposite Burgers vector [17]. A dynamic equilibrium between the number of dislocations emitted by sources and the number of dislocations annihilated in these boundaries is established. These LABs are effectively pinned by a dispersion of coherent  $Al_3(Sc,Zr)$  particles [11,13]; therefore, no coalescence and the straightening of crystallite delimited by these boundaries occur with strain. Transformation of this structure to grains may occur only through the conversion of these separate LABs to GNBs, followed by the appearance of HAB segments (Fig. 10) [35]. Multiple slip in disoriented crystallites leads to the deviation of orientations of numerous subgrains from the stable  $B_0 / \bar{B}_0$  components (Fig. 10). As a result, a significant difference in slip system activity may appear in a pair of neighbor subgrains (no. 1 and no. 2 in Fig. 10) [19,20,40]. Boundary segments between neighboring subgrains with a difference in orientations start to play the role of a GNB and

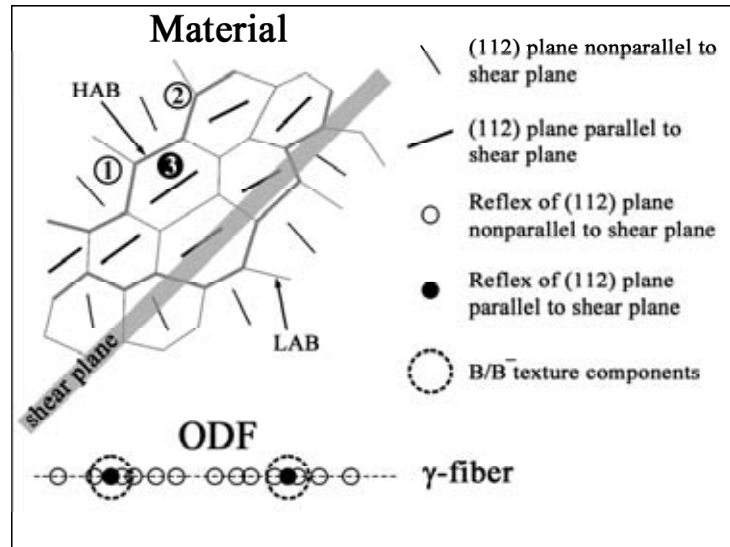


Fig. 10. Schematic presentation of appearance of  $\gamma$ -fiber.

increase their misorientation with a high rate (no. 1 and no. 2 in Fig. 10). This conversion modifies the dynamic equilibrium in following way: the number of dislocations emitted by sources is nearly equal to the number of dislocations trapped by GNBs and increasing their misorientation. This behavior provides grain refinement and the growth of subgrains/(sub)grains at  $\varepsilon \geq 6$  (Fig. 6b) through balancing of the boundary tension [11]. In addition, stress-driven splitting and migration of boundaries with low- and high-angle misorientation owing to grain boundary sliding accelerates transformation of LAB segments to HABs ones [41,42]. It is worth noting that this alloy exhibit superior superplastic ductility at a temperature of 300 °C and high strain rates typical for ECAP [1,27].

The formation of a 3D network of GNBs occurs for orientations close to the stable components after the first pass through the intersections of MSBs belonging to two non-coplanar families [15,23,24]. This Type 3 structure easily converts to granular structure, which leads to complete recrystallization in some areas at low strains. However, the fraction of these areas is low. The increase in recrystallized fraction at  $\varepsilon \geq 2$  is attributed to the transition from Type 2 structure appearing in the unstable orientations to Type 3 structure appearing in stable orientation close to the  $B_0 / \bar{B}_0$  components (no. 3 in Fig. 10). This orientation is located along the  $\gamma$ -fiber. However, a (sub)grain with the  $B_0 / \bar{B}_0$  orientation is surrounded by other (sub)grains having unstable orientations (no. 3 in Fig. 10). As a result, all boundary segments of the (sub)grains with the  $B_0 / \bar{B}_0$  orientation are in fact highly misoriented GNBs, and this (sub)grain transforms to grains

easily. Therefore, the formation of the  $\gamma$ -fiber (Fig. 8c-8g) is associated with increases in the  $\theta_{av}$  and  $V_{HAB}$  values in the strain interval 4-8 (Fig. 6d) [15]. The formation of separate segments of HABs (Fig. 10) for orientations belonging to the  $\gamma$ -fiber promotes the gradual transformation of LABs into HABs with strain and enables the eventual formation of a fully recrystallized structure.

Thus, the formation of GNBs and their subsequent transformation to planar subboundaries, which easily increase misorientation with strain, play a vital role in grain refinement in the Al-Mg-Sc-Zr alloy at intermediate temperature during ECAP in all orientations. The localized simple shear under ECAP, which highly promotes the evolution of GNBs, is extremely important for the CDRX process in aluminum alloys.

## 5. CONCLUSIONS

1. In the Al-5.4Mg-0.2Sc-0.09Zr alloy, the ECAP through route  $B_c$  up to a total strain of  $\sim 12$  leads to the formation of a fully recrystallized structure with an average grain size of  $\sim 0.8 \mu\text{m}$ . The formation of geometrically necessary boundaries plays a vital role in the initiation of continuous dynamic recrystallization. The initial grain orientation determines the formation of 3D networks of geometrically necessary boundaries. Three types of dislocation boundary structures were classified based on the dependence on the orientation of the initial grains.

2. Three well-defined stages in the strain dependence of the average misorientation,  $\theta_{av}$ , and the fraction of high-angle boundaries were found. For  $\varepsilon \sim 1$ , these

values increase rapidly (Stage I) and remain nearly unchanged in strain interval 1-2 (Stage II). The density of individual lattice dislocations continuously increases by a factor of  $\sim 12$  to  $\rho \sim 1.2 \times 10^{14} \text{ m}^{-2}$  at  $\varepsilon \sim 2$ . Continuous lattice rotation,  $\theta$ , indicating a great polarity of the accumulated dislocations, also gradually increases up to this strain. The steep increases in the  $\theta_{av}$  and  $V_{HAB}$  values occur with increasing strain in Stage III. A dynamic equilibrium between the number of dislocations emitted by the sources and the number of dislocations trapped by the boundaries is established, and no change in dislocation density occurs.

3. In the grain rotate toward stable orientations belonging to the  $\alpha$ - and  $\beta$ -fibers, the lamellar structure appears due to the formation of both microshear bands (MSBs) enclosed by a pair of geometrically necessary boundaries (GNBs) and/or ribbons bounded by initial boundaries from one side and planar GNBs from the opposite side. Transformation of 2D lamellar structure to 3D crystallites occurs through the intersection of primary MSBs and/or the ribbons by secondary MSBs.

4. Grain refinement in grains with unstable orientations is associated with the appearance of a new type of shear texture called  $\gamma$ -fiber, which is an axial  $\{112\}$  texture orientation around the transverse direction. This  $\gamma$ -fiber runs through the stable components. Continuous propagation of GNBs through network of incidental dislocation boundaries leads to the formation of 3D networks of high-angle boundaries and eventual formation of a fully recrystallized structure.

## ACKNOWLEDGMENTS

The financial support received from the Ministry of Education and Science, Russia, (Belgorod State University project №11.1533.2014/K) is acknowledged. The authors are grateful to the personnel of the Joint Research Centre at Belgorod State University for their assistance with the instrumental analysis.

## REFERENCES

- [1] R.Z. Valiev and T.G. Langdon // *Prog. Mater. Sci.* **51** (2006) 881.
- [2] T. Sakai, A. Belyakov, R. Kaibyshev, H. Miura and J.J. Jonas // *Prog. Mater. Sci.* **60** (2014) 130.
- [3] P.J. Apps, M. Berta and P.B. Prangnell // *Acta Mater.* **53** (2005) 499.
- [4] W. Skrotzki, N. Scheerbaum, C.-G. Oertel, H.-G. Brokmeier, S. Suwas and L.S. Toth // *Acta Mater.* **55** (2007) 2211.
- [5] Ch. Xu, M. Furukawa, Z. Horita and T.G. Langdon // *Mater. Sci. Eng. A* **398** (2005) 66.
- [6] Ch. Xua, Z. Horita and T.G. Langdon // *Mater. Sci. Eng. A* **528** (2011) 6059.
- [7] R. Kaibyshev, K. Shipilova, F. Musin and Y. Motohashi // *Mater. Sci. Eng. A* **396** (2005) 341.
- [8] I. Mazurina, T. Sakai, H. Miura, O. Sitdikov and R. Kaibyshev // *Mater. Sci. Eng. A* **473** (2008) 297.
- [9] I. Mazurina, T. Sakai, H. Miura, O. Sitdikov and R. Kaibyshev // *Mater. Sci. Eng. A* **486** (2008) 662.
- [10] O. Sitdikov, T. Sakai, E. Avtokratova, R. Kaibyshev, K. Tsuzaki and Y. Watanabe // *Acta Mater.* **56** (2008) 821.
- [11] F.J. Humphreys and M. Hatherly, *Recrystallization and related annealing phenomena* (Oxford, Elsevier, 2005).
- [12] T.C. Schulthess, P.E.A. Turchi, A. Gonis and T.-G. Nieh // *Acta Mater.* **46** (1998) 2215.
- [13] I. Nikulin, A. Kipelova, S. Malopheyev and R. Kaibyshev // *Acta Mater.* **60** (2012) 487.
- [14] O. Sitdikov, E. Avtokratova, T. Sakai and K. Tsuzaki // *Metall. Mater. Trans. A* **44** (2013) 1087.
- [15] M. Gazizov, S. Malopheyev and R. Kaibyshev // *J. Mater. Sci.* **50** (2015) 990.
- [16] Y. Estrin and A. Vinogradov // *Acta Mater.* **61** (2013) 782.
- [17] P.J. Hurley and F.J. Humphreys // *Acta Mater.* **51** (2003) 1087.
- [18] N. Afrin, M.Z. Quadir, W. Xua and M. Ferry // *Acta Mater.* **60** (2012) 6288.
- [19] G. Winther, D.J. Jensen and N. Hansen // *Acta Mater.* **45** (1997) 5059.
- [20] D.A. Hughes, N. Hansen and D.J. Bammann // *Scripta Mater.* **48** (2003) 147.
- [21] Ch. Hong, X. Huang and G. Winther // *Phil. Mag.* **93** (2013) 3118.
- [22] D.A. Hughes and N. Hansen // *Acta Mater.* **45** (1997) 3871.
- [23] X. Huang and G. Winther // *Phil. Mag.* **87** (2007) 5189.
- [24] X. Huang and G. Winther // *Phil. Mag.* **87** (2007) 5215.
- [25] S. Gourdet and F. Montheillet // *Mater. Sci. Eng. A* **283** (2000) 274.
- [26] A. Belyakov, T. Sakai and R. Kaibyshev // *Metall. Mater. Trans. A* **29** (1998) 161.

- [27] R. Kaibyshev, E. Avtokratova, A. Apollonov and R. Davies // *Scr. Mater.* **54** (2006) 2119.
- [28] R. Kaibyshev, F. Musin, E. Avtokratova and Y. Motohashi // *Mater. Sci. Eng. A* **392** (2005) 373.
- [29] A. Mogucheva, E. Babich, B. Ovsyannikov and R. Kaibyshev // *Mater. Sci. Eng. A* **560** (2013) 178.
- [30] P.W.J. Mckenzie and R. Lapovok // *Acta Mater.* **58** (2010) 3198.
- [31] P.B. Hirsch, A. Howie, R.B. Nicholson, D.W. Pashley and M.J. Whelan, *Electron Microscopy of Thin Crystals* (2nd ed., Krieger, New York, 1977).
- [32] I.J. Beyerlein and L.S.Toth // *Prog. Mater. Sci.* **54** (2009) 427.
- [33] I.Ovid'ko and N.V. Skiba // *Rev. Adv. Mater. Sci.* **35** (2013) 96.
- [34] J.K. Mackenzie // *Biometrika* **45** (1958) 229.
- [35] S. Gourdet and F. Montheillet // *Acta Mater.* **51** (2003) 2685.
- [36] D. Ponge and G. Gottstein // *Acta Mater.* **46** (1998) 69.
- [37] S.V. Bobylev and I.A. Ovid'ko // *Acta Mater.* **88** (2015) 260.
- [38] M. Biberger and W. Blum // *Phil. Mag. A* **65** (1992) 757.
- [39] A.A. Gazdera, W. Cao, Ch.H.J. Davies and E.V. Pereloma // *Mater. Sci. Eng. A* **497** (2008) 341.
- [40] Q. Xue, I.J. Beyerlein, D.J. Alexander and G.T. Gray III // *Acta Mater.* **55** (2007) 655.
- [41] S. V. Bobylev, N. F. Morozov, I. A. Ovid'ko // *Phys. Rev. B* **84** (2011) 094103.
- [42] R. Kaibyshev, A. Goloborodko, F. Musin, I. Nikulin and T.Sakai // *Mater. Trans.* **43** (2002) 2408.